

Functional Data Analysis using a Topological Summary Statistic: the Smooth Euler Characteristic Transform

Lorin Crawford^{1-3,†}, Anthea Monod^{4,†}, Andrew X. Chen⁴, Sayan Mukherjee⁵⁻⁸, and Raúl Rabadán⁴

1 Department of Biostatistics, Brown University, Providence, RI, USA

2 Center for Statistical Sciences, Brown University, Providence, RI, USA

3 Center for Computational Molecular Biology, Brown University, Providence, RI, USA

4 Department of Systems Biology, Columbia University, New York, NY, USA

5 Department of Statistical Science, Duke University, Durham, NC, USA

6 Department of Computer Science, Duke University, Durham, NC, USA

7 Department of Mathematics, Duke University, Durham, NC, USA

8 Department of Bioinformatics & Biostatistics, Duke University, Durham, NC, USA

† Corresponding E-mail: lorin_crawford@brown.edu; am4691@cumc.columbia.edu

Abstract

In medical imaging informatics, the quantification of shape features for statistical analyses is an important problem. To this end, we introduce a novel statistic, the smooth Euler characteristic transform (SECT), which is designed to include shape information as covariates in regression models by representing shapes and surfaces as a collection of curves. Due to its well-defined inner product structure, the SECT can be used in a wider range of functional and nonparametric modeling approaches than other previously proposed topological summary statistics. We apply the SECT to a cancer radiomics study and demonstrate that, for tumors assayed by magnetic resonance imaging (MRI), shape quantification via the SECT is a better predictor of clinical outcomes in patients with glioblastoma multiforme (GBM) than molecular assays and other tumor shape quantification methods. Specifically, we demonstrate that SECT features alone explain more of the variance in patient survival than gene expression, volumetric features, and morphometric features.

1 Introduction

The field of radiomics is focused on the extraction of quantitative features from medical magnetic resonance images (MRIs), typically constructed by tomography and digitally stored as shapes or surfaces. The problem of quantifying geometric features from a shape in a way that is amenable to statistical modeling has been a long-standing and fundamental challenge in both statistics as well as radiomics. In this paper, we address this problem by designing a novel statistic, the smooth Euler characteristic transform (SECT), in order to integrate shape information into standard functional regression models. The main idea behind the SECT is that physical properties from images and three-dimensional objects can be represented as a collection of smooth curves. This transformation to a collection of curves is key because it allows the use of well-developed statistical tools from functional data analysis (FDA) to model shapes. Hence, the statistical contribution of this paper is twofold: (i) a novel summary statistic for quantifying shape features, and (ii) a functional regression framework that allows the integration of shape information as covariates.

Much of radiomic research has been driven by applications in oncology, and in this study we will apply the SECT to a predictive analysis of survival outcomes for patients with glioblastoma multiforme (GBM) — a glioma that materializes into aggressive, cancerous tumor growths within the human brain. Specifically, we will focus on a select cohort with both publicly available MRI images from The Cancer

Imaging Archive (TCIA) [1, 2], as well as matched genomic and clinical data collected by The Cancer Genome Atlas (TCGA) [3]. Through an extensive predictive analysis, we demonstrate a clinically relevant connection between the topology of brain malignancies and the variation of survival-based outcomes that are driven by molecular heterogeneity.

The remainder of this paper is organized as follows. In Section 2, we outline the theoretical concepts used to develop the SECT and highlight its statistical utility. In Section 3, we detail how regression methodologies for functional covariates are naturally suited to model the curves resulting from the SECT. This connection with functional data allows us to specify a general regression model that uses shape information and takes on a form that is known to be particularly powerful when conducting predictive inference. For this particular case study, we focus on Gaussian process (GP) regression with Markov chain Monte Carlo (MCMC) inference. In Section 4, we apply the GP modeling framework to predict the clinical outcomes of GBM patients using gene expression data, existing morphometric and volumetric tumor image quantifications, and our proposed topological summaries. Here, we perform a comparative study between each covariate type across different regressions generated by various covariance functions. Finally, in Section 5, we close with a discussion on possible future research.

2 Representing Shapes as Functional Covariates

In this section, we will develop a summary statistic that captures shape information from MRI images of GBM tumors — which will then be used as covariates in a regression model. The key conceptual component is to construct these statistics as a function that maps shapes into a Hilbert space. This function has two important properties: (i) it is injective, and (ii) it admits a well-defined inner product structure. The inner product structure is important as it allows us to adapt ideas from functional data analysis to specify general regression models that use shape summary statistics as predictor variables.

2.1 Background on Summary Statistics for Shape Data

The classic model for shape statistics represents shapes as a collection of landmark points [4–6]. This data representation was implemented partly due to the limited image processing technology of the time. Current imaging technologies have since greatly improved and now allow three-dimensional shapes to be represented as meshes — which are collections of vertices, edges, and faces. Figure A1 depicts an example of a mesh representation for a brain tumor and ventricles. Recently, methods have been developed to generate automated geometric morphometrics for mesh representations [7–10]. However, despite these advancements, both user-specified and automated landmark-based methods for geometric morphometrics are known to suffer from structural errors when comparing shapes that are highly dissimilar. Some examples of structural errors include: inaccurate pairwise correspondences between landmarks, alignment problems between dissimilar shapes, and global inconsistency of pairwise mappings. These structural errors tend to accumulate as the number of landmark points imposed on each shape increases. A high number of landmark points is often required to accurately capture shape information, especially when analyzing diverse collections [11]. Such complications, together with the advancement in both imaging technology and computational tools to process imaging data, make general landmark-based approaches less attractive.

Most recently, an approach known as the persistent homology transform (PHT) was developed to comprehensively address issues induced by landmark-specification, and to maintain robust quantification performance for highly dissimilar and non-isomorphic shapes [12]. The PHT allows for the comparison of shapes without requiring landmarks. Unfortunately, the PHT is a collection of persistence diagrams — multiscale topological summaries used extensively in topological data analysis (TDA). This is important because the geometry of the resulting summary statistics does not allow for an inner product structure that is amenable to (generalized) functional data models [13]. Our contribution, the smooth Euler

characteristic transform (SECT), builds upon the theory of the PHT to propose a topological summary statistic that is constructed to integrate shape information in regression-based methods. This proves to be particularly useful in our case study on predicting clinical outcomes in GBM.

2.2 Homology and Persistence

We begin by developing an intuition for *persistent homology* [14, 15], which is a foundational concept in TDA. Briefly, persistent homology can be viewed as the data analytic counterpart to *homology* — a theoretical component from algebraic topology, where the goal is to develop methods to count occurrences of geometric patterns in arbitrary topological spaces (i.e. generalizations of geometric objects). Therefore, homology groups provide a mathematical language for describing holes in a given topological space. The motivation behind classical algebraic topology is to then use these holes to distinguish or suggest similarities between different topological spaces. For a more detailed review and theoretical discussion of these concepts, see the Appendix.

Homology. Homology is particularly relevant to our application and case study in GBM. Intuitively, not only does it describe contrasting physical tumor characteristics, but it also implicitly captures some information about the stage of disease progression. For example, *necrosis* is a form of cell injury which results in the premature death of cells. *Multifocality* is a radiological observation where individual tumor cells separate from the main mass and disperse elsewhere within the brain. From an imaging perspective, necrotic regions show up as dark regions (or holes) within a tumor; while multifocal tumors appear as segregated masses. Examples of both necrosis and multifocality captured by MRI images are shown in Figure A3. It has been suggested that the more necrosis or multifocality there is in a GBM tumor, the more aggressive the disease [16, 17]. Applying homology to radiomic studies not only identifies such phenomena, but also tracks the number of times they occur; thereby, providing some measure of disease severity.

Theoretically, homology is indexed by integers: the 0th-degree homology captures the number of connected components in the shape, the 1st-degree homology captures the number of loops, and the 2nd-degree homology captures the number of voids. In the context of our GBM application, degree 0 homology corresponds to tumor masses and lesions, while degrees 1 and 2 homology correspond to necrosis, depending on whether we consider analyzing the 2-dimensional image slices from an MRI or the 3-dimensional tumor as a whole, respectively.

Despite its intuitive description, computing homology can be challenging. To this end, it is often convenient to represent the shape as a discrete union of simple building blocks, “glued” together in a combinatorial fashion. An important example of such building blocks are *simplices*, which are skeletal elements such as vertices, edges, triangles (faces), tetrahedra, and other higher dimensional structures. A *simplicial complex* K is a collection of simplices and represents the discretization of a shape or tumor. Meshes that represent three-dimensional shapes are particular examples of finite simplicial complexes (again see Figure A1). There are two key interests in discretizing shapes into simplicial complexes. First, discretization is essential for applying these abstract concepts to data science where any given dataset will necessarily be finite; and second, there exist efficient algorithms to compute homology for such discretizations. The notation we use in this paper denotes the k^{th} homology group, for a simplicial complex K , as $H_k(K)$. This corresponds to the collection of the k -dimensional elements of the simplicial complex. For example, 0-“holes” are the collection of vertices of the simplicial complex (or connected components of a shape, such as the masses and lesions of a tumor).

Persistent Homology. *Persistent homology* applies homology to data by continuously tracking the evolution of homology in the data at different scales (or resolutions). Alternatively, it can be seen as a way to extract and summarize geometric information. A statistical analogy of persistent homology is

single-linkage clustering: data points are grouped together in a sequential manner by first considering the shortest distance between clusters, to then forming larger and larger clusters, until finally all elements are combined into a single giant cluster. In terms of homology as described above, these clusters are connected components. Connected components represent the most basic “hole” tracked in the homology of a shape or surface — they are the 0th-degree homology, denoted by H_0 . The result of single-linkage clustering can be summarized via a dendrogram, which is a profile that encodes the clusterings at all distance thresholds simultaneously. Persistent homology may be thought of as a generalized procedure akin to single-linkage clustering that is valid not only for connected components, but also for higher order topological features (holes).

In persistent homology, the analog to the distance that determines how clusters grow and merge is the index t of a *filtration*. A filtration is a collection of simplicial complexes $\{K_t\}$ where the index t induces totally ordered sets, $K_i \subseteq K_j$ for $i < j$. As t increases, the sequence of simplicial complexes $\{K_t\}$ also changes and grows — just as the agglomerate clustering behavior changes and grows as the distance between clusters increase. In other words, in persistent homology, the index t of the filtration $\{K_t\}$ tracks the scale according to which the “shape” of the data evolves. The individual elements K_t of the filtration (collection) $\{K_t\}$ correspond to the clusters present at each step of the clustering process. The shape information at each scale t is encoded by the homology groups $H_k(K_t)$ of the simplicial complex K_t . More specifically, H_0 corresponds to the vertices, H_1 corresponds to edges, and H_2 corresponds to the faces of the simplicial complex or discretized shape. An example of a filtration is depicted in Figure 1. Here, the index t is the height function in the vertical direction, and we see the evolution of vertices, edges, and a face appearing sequentially with height. In the same way that the actual data points present at the beginning of the procedure in a clustering analysis do not disappear as the clustering behavior grows coarser at larger distances, structures (such as vertices) that appear at the beginning of a filtration do not disappear as the filtration evolves. Higher order structures are revealed with increasing t .

The final output produced from computing persistent homology is analogous to the dendrogram summarizing single-linkage clustering. After computing persistent homology, we get a collection of intervals for each degree of homology, where each interval represents a k -dimensional topological feature (e.g. a connected component, loop, or void for a general shape) that is “born” at the parameter value given by the left endpoint of the interval, and “dies” at the value at the right endpoint. The length of the interval corresponds to how long the topological feature “lives,” or persists. In this paper, we consider these intervals to be represented by a *persistence diagram*. Persistence diagrams treat the start and end points of each interval as an ordered pair, and displays them as plotted points on a plane where the x -axis corresponds to birth time and the y -axis is the death time. Thus, one can consider a persistence diagram as a collection of points above the diagonal, with the set of points on the diagonal having infinite multiplicity (for regularity conditions; see the Appendix for further detail). The persistence diagram is also analogous to the dendrogram since it encodes the evolution of the k^{th} homology group at all filtration index values simultaneously.

Persistent Homology Transform. The PHT captures shape information by collecting persistence diagrams of all degrees of homology, for all possible orientations of the shape. More formally, for a d -dimensional shape, the PHT results in d -many persistence diagrams arising from height function filtrations over infinitely many direction vectors on the surface of the sphere. The space of persistence diagrams is a complicated, but theoretically well-defined probability space [18]. In particular, it is a metric space, meaning that distances between persistence diagrams may be defined. This is important because distances between PHT summary statistics provide a way of comparing shapes. The injectivity of the PHT for 2- and 3-dimensional shapes [12] — in other words, the one-to-one relation between the shape itself and its infinite collection of persistence diagrams — guarantees that the PHT effectively summarizes all relevant information about the shape.

Considering all possible directions on the surface of the sphere to summarize shape information is

particularly well-suited to our radiomics application. Here, MRI scans of the brain are known to be subject to noise. An example of such noise can stem from the positioning of a patient’s head, which could potentially vary both between patients and individual scans, causing image registration issues. Considering all directions on the surface of the sphere bypasses this problem, and incorporates perturbations directly into the statistic. This is an important feature of the PHT that we retain in the development of the SECT. We expand upon the PHT to produce a collection of continuous, piecewise linear functions that live in Hilbert space, \mathbb{L}^2 . The corresponding inner product structure inherent to Hilbert spaces allows us to apply the SECT to a much broader set of statistical methodologies. Note that for select covariance functions the PHT can be adapted to nonparametric statistical models [19–21], but this class is notably limited.

2.3 Smooth Euler Characteristic Transform

While the SECT uses the same underlying mathematical principles as the PHT, it alternatively produces a collection of continuous, piecewise linear functions that can be considered an element in the Hilbert space. The SECT implements persistent homology via the Euler characteristic (EC), a topological invariant that appears in many branches of mathematics. In terms of homology, the EC counts the ranks of the homology groups (i.e. the Betti numbers, β_k , for the k^{th} homology group H_k) in an alternating sum — thus, reducing how holes in a topological space are described from an algebraic group structure to merely an integer.

Definition 1. Let X be a general, arbitrary topological space, $H_k(X)$ be the k^{th} homology group of X , and β_k be the rank of $H_k(X)$. The Euler characteristic (EC) $\chi(X)$ of X is the alternating sum

$$\chi(X) = \beta_0 - \beta_1 + \beta_2 - \beta_3 + \dots = \sum_{k=0}^{\infty} (-1)^k \beta_k.$$

For a discretized shape or surface in three dimensions represented as a simplicial complex K , the EC may be analogously defined by the number of simplices in K by

$$\chi(K) = V - E + F$$

where V , E , and F are the numbers of vertices (0-simplices), edges (1-simplices), and faces (2-simplices), respectively.

Just as homology may be augmented to persistent homology by considering a filtration, ECs may also be calculated with respect to a filtration. The result is an EC curve, which tracks the progression of the EC as a function with respect to the filtration. Let the dimension $d = \{2, 3\}$, and fix a direction ν on the surface of the unit sphere S^{d-1} , $\nu \in S^{d-1}$. Next, let \mathcal{M}_{d-1} be the set of all closed, compact subsets (shapes) embedded in \mathbb{R}^d that can be represented in a finite, discrete manner as simplicial complexes [22]. Next, denote K to be the simplicial complex representation of $M \in \mathcal{M}_{d-1}$. The *sublevel set filtration* of K_ν parameterized by a height $r(\bullet)$ is then

$$K(\nu)_r = \{x \in K : x \cdot \nu \leq r\}. \tag{1}$$

The parameter height function $r_\nu(\bullet)$ is

$$\begin{aligned} r : K \times S^{d-1} &\rightarrow \mathbb{R} \\ \{x\} &\mapsto x \cdot \nu. \end{aligned} \tag{2}$$

Denote the extremal heights from this filtration by

$$a_\nu := \min\{r_\nu(x) : x \in K\},$$

$$b_\nu := \max\{r_\nu(x), x \in K\}.$$

We use the subscript notation to denote the simplicial complex representation K of a shape M in the direction ν as K_ν for $d = \{2, 3\}$. Similarly, we use the superscript notation to denote the simplicial complex of K_ν generated by sublevel set filtration in Equation (1) defined by Equation (2), K_ν^x .

Definition 2. The *EC curve* of K (which discretizes M) in the direction ν is defined by

$$\begin{aligned} \chi_\nu^K : [a_\nu, b_\nu] &\rightarrow \mathbb{Z} \subset \mathbb{R} \\ x &\mapsto \chi(K_\nu^x). \end{aligned} \quad (3)$$

The EC curve tracks the evolution of the EC up to (and including) the largest subcomplex of K_ν^x contained in the sublevel set $r_\nu^{-1}((-\infty, x])$. See Figures 2(a) and 2(b) for an illustrative example of the evolution of the EC on the two-dimensional contour of a hand. Here, the direction is the horizontal direction to the right of the y -axis. The value of the EC changes as the sweep over the palm first reveals the thumb, and then the separation between the ring and pinky fingers, followed very shortly by the separation between the index and middle fingers, and so on. The EC curve of this filtration is plotted in Figure 2(b).

Briefly referencing the robust summarizing technique of the PHT, which considers all directions on the surface of the sphere, gives the following definition in terms of ECs.

Definition 3 (Previously in [12]). In considering a directional sweep over the surface of the sphere S^{d-1} , and calculating the corresponding EC curves χ_ν^K of the finite simplicial complex representations K_ν for every direction $\nu \in S^{d-1}$, the *Euler characteristic transform (ECT)* is defined as follows:

$$\begin{aligned} \text{ECT}(K) : S^{d-1} &\rightarrow \mathbb{Z}^{\mathbb{R}} \\ \nu &\mapsto \chi(K_\nu). \end{aligned} \quad (4)$$

In other words, the ECT of a shape collects EC curves of the shape, over all directions on the surface of the sphere.

The EC curve in Equation (3) and its corresponding ECT in Equation (4) are piecewise constant, integer-valued functions. These discontinuities can affect the stability of this representation (e.g. see Figure 2(b), where there are sharp jumps in the curve). We therefore propose a reformulation of Equation (4) that allows for a type of summary that can be used in a wider range of statistical analyses. We do this by smoothing the function via the following procedure. First, take the mean value of the EC curve $\bar{\chi}_\nu^K$ over $[a_\nu, b_\nu]$. Next, we subtract this mean from the value of the EC curve $\chi_\nu^K(x)$ at every $x \in [a_\nu, b_\nu]$. The result is a centered EC curve in the direction $\nu \in S^{d-1}$,

$$\begin{aligned} Z_\nu^K : [a_\nu, b_\nu] &\rightarrow \mathbb{R} \\ x &\mapsto \chi_\nu^K(x) - \bar{\chi}_\nu^K. \end{aligned} \quad (5)$$

We set the value of Z_ν^K to be zero outside the interval $[a_\nu, b_\nu]$ by default. We then integrate the curve to specify the following construct.

Definition 4. The *centered, cumulative Euler characteristic curve* or *smooth Euler characteristic curve (SEC)*, for a fixed direction $\nu \in S^{d-1}$, is defined for all $y \in \mathbb{R}$ as

$$\begin{aligned} \text{SEC}(K) : \mathbb{R} &\rightarrow \mathbb{L}^2 \\ F_\nu^K(y) &:= \int_{-\infty}^y Z_\nu^K(x) dx \end{aligned} \quad (6)$$

The SEC is a continuous, piecewise linear function with compact support $[a_\nu, b_\nu]$ by construction. Therefore, it is an element of the Hilbert space \mathbb{L}^2 of square integrable functions on \mathbb{R} . The counterpart to Figure 2(b), smoothed by the procedure described above resulting in the SEC, is visually illustrated in Figure 2(c). We now formally define the smooth Euler characteristic transform.

Definition 5. The *smooth Euler characteristic transform (SECT)* for a simplicial complex K of a shape $M \subset \mathbb{R}^d$, with $d = \{2, 3\}$, is the map

$$\begin{aligned} \text{SECT}(K) : S^{d-1} &\rightarrow \mathbb{L}^2[a_\nu, b_\nu] \\ \nu &\mapsto F_\nu^K(b_\nu) \end{aligned} \quad (7)$$

for all $\nu \in S^{d-1}$. Each curve F_ν^K is also an element in the Hilbert space \mathbb{L}^2 . The following metric can therefore be used to define distances between two simplicial complexes (discrete shape representations) K_1 and K_2 ,

$$\text{dist}_{\mathcal{M}_{d-1}}^{\text{SECT}}(K_1, K_2) := \left(\int_{S^{d-1}} \|F_\nu^{K_1} - F_\nu^{K_2}\|^2 d\nu \right)^{1/2}. \quad (8)$$

The advantage of the SECT over the PHT is that SECT summaries are a collection of curves and have a Hilbert space structure. This means that their structure allows for quantitative comparisons using the full scope of functional and nonparametric statistical methodology. The SECT is also an injective map and the following corollary is an immediate consequence of previous results [12].

Corollary 1. *The smooth Euler characteristic transform is injective for two- and three-dimensional shapes, i.e. when the domain is \mathcal{M}_{d-1} for $d = \{2, 3\}$.*

It is important to note that enough directions $\nu \in S^{d-1}$ must be taken for this corollary to hold since, for any one fixed direction, it is not true that the EC curve (upon which the SECT construction depends) is injective. An illustration of this fact is depicted in Figure A2. To determine the number of directions to use in practice, we perform a sensitivity analysis with many different combinations of numbers of directions and sublevel sets. In our application of interest and case study, we find prediction results (with SECT features as predictor variables) to be reasonably robust to our final choice of numerical parameters.

3 Functional Regression Models with Shape as Covariates

In the previous section, we formally specified the SECT which allows us to map shapes into a space that: (i) is represented by collection of curves, and (ii) has a well-defined inner product structure. We will now adapt ideas from functional data analysis (FDA) to specify a general regression model that uses topological summary statistics as covariates. The goal of FDA is to model data that are continuous functions (e.g. curves, response surfaces, or images) [23–27]. The key idea here is that these functions can be considered as elements in a Hilbert space for which one can specify statistical models using stochastic processes [28–31]. In this paper, we will use a class of stochastic processes that is often referred to as Gaussian processes (GPs) [32–34].

3.1 Gaussian Process Regression

Denote the SECT representation of a GBM MRI scan as $\mathbf{F}(t) = \{F_\nu\}_{\nu=1}^m$ measured over m directions. A functional linear model considers a continuous response variable \mathbf{y} and covariates that are square integrable functions $\mathbf{F}(t)$ on the real interval \mathcal{T} , where $t \in \mathcal{T}$ under the following parametric form [23]

$$\mathbf{y} = \langle \mathbf{F}(t), \boldsymbol{\alpha}(t) \rangle + \boldsymbol{\varepsilon}, \quad \boldsymbol{\varepsilon} \sim \mathcal{N}(\mathbf{0}, \tau^2 \mathbf{I})$$

where the residual noise $\boldsymbol{\varepsilon}$ is assumed to follow a multivariate normal distribution with mean zero and scaled variance parameter τ^2 with \mathbf{I} being used to denote the identity matrix. Notice that similar to traditional linear regression models, $\boldsymbol{\alpha}(t)$ is an unknown smooth parameter function that is now square integrable on the domain \mathcal{T} , and $\langle \bullet, \bullet \rangle$ denotes a well-defined inner product. In the context of our radiomic case study, the assumption of a linear relationship between the response variable \mathbf{y} and

functional covariates $\mathbf{F}(t)$ may be too restrictive. For example, when modeling the topological landscape of brain tumors (as we will do in Section 4), it is reasonable to assume that interactions between modes of brain activity extend well beyond additivity [35]. As a result, we will formulate a general functional regression model that has the flexibility to incorporate possible nonlinear interactions. The methodology we will use is Gaussian process (GP) regression.

There are two key characteristics of a GP regression model. The first key element is a positive definite covariance function, $\sigma : \mathbb{L}^2 \times \mathbb{L}^2 \rightarrow \mathbb{R}$, where again \mathbb{L}^2 is the Hilbert space of the SECT functional covariates such that $\mathbf{F}(t) \in \mathbb{L}^2$. The second key element is the reproducing kernel Hilbert space (RKHS) that is induced by the covariance function. Given the eigenfunctions $\{\psi_j\}_{j=1}^\infty$ and eigenvalues $\{\lambda_j\}_{j=1}^\infty$ of the finite integral operator defined by the covariance function [36], we have

$$\int_{\mathcal{T}} \sigma(\mathbf{u}, \mathbf{v}) d(\mathbf{u}, \mathbf{v}) < \infty, \quad \lambda_j \psi_j(\mathbf{u}) = \int_{\mathcal{T}} \sigma(\mathbf{u}, \mathbf{v}) \psi_j(\mathbf{v}) d\mathbf{v},$$

where $\mathbf{u} = \mathbf{u}(t)$ and $\mathbf{v} = \mathbf{v}(t)$, and an RKHS can be formally defined as the closure of a linear combination of basis functions $\{\sqrt{\lambda_j} \psi_j(\mathbf{v})\}_{j=1}^\infty$ [33]. One may conduct inference in an RKHS by assuming a Gaussian process prior distribution over the functional covariates directly [37],

$$f(\mathbf{F}_i(t)) \sim \mathcal{GP}(\mu(\mathbf{F}_i(t)), \sigma(\mathbf{F}_i(t), \mathbf{F}_\ell(t))), \quad \ell = 1, \dots, n \quad (9)$$

where $f(\bullet)$ is a smooth operator from \mathbb{L}^2 to \mathbb{R} that is completely specified by its mean function and positive definite covariance function, $\mu(\bullet)$ and $\sigma(\bullet, \bullet)$, respectively. Recall from Section 2 that, in practical applications, there are a finite number of observed topological summary statistics taken from a given geometric object. Therefore, if we condition on these finite set of locations, the prior distribution in Equation (9) may be represented as a multivariate normal [38]. Consider the following joint ‘‘weight-space’’ probabilistic regression model to complete our specification [37],

$$\mathbf{y} = \mathbf{f} + \boldsymbol{\varepsilon}, \quad \mathbf{f} \sim \mathcal{N}(\mathbf{0}, \boldsymbol{\Sigma}), \quad \boldsymbol{\varepsilon} \sim \mathcal{N}(\mathbf{0}, \tau^2 \mathbf{I}), \quad (10)$$

where $\mathbf{f} = [f(\mathbf{F}_1(t)), \dots, f(\mathbf{F}_n(t))]^\top$ is now assumed to come from a multivariate normal with mean $\mathbf{0}$ and covariance matrix $\boldsymbol{\Sigma}$ with elements computed as $\Sigma_{i\ell} = \sigma(\mathbf{F}_i(t), \mathbf{F}_\ell(t))$.

3.2 Posterior Predictive Inference

We now formally describe how to conduct posterior predictive inferences on clinical phenotypic traits for unobserved patients. Assume that we have received a set of new brain tumors and have computed their corresponding topological summary statistics. We can write the joint distribution between the observed patient responses (\mathcal{S}) and the function values taken at the test images (\mathcal{T}), under the prior in Equation (9), as

$$\begin{pmatrix} \mathbf{y} \\ \mathbf{f}_T \end{pmatrix} \sim \mathcal{N} \left(\begin{pmatrix} \mathbf{0} \\ \mathbf{0} \end{pmatrix}, \begin{pmatrix} \boldsymbol{\Sigma}_{SS} + \tau^2 \mathbf{I} & \boldsymbol{\Sigma}_{ST} \\ \boldsymbol{\Sigma}_{TS} & \boldsymbol{\Sigma}_{TT} \end{pmatrix} \right) \quad (11)$$

where $\boldsymbol{\Sigma}_{TS}$ and $\boldsymbol{\Sigma}_{SS}$ are sub-matrices that are found by first computing $\tilde{\boldsymbol{\Sigma}} = [\boldsymbol{\Sigma}_{SS}; \boldsymbol{\Sigma}_{ST}; \boldsymbol{\Sigma}_{TS}; \boldsymbol{\Sigma}_{TT}]$ and appropriately partitioning $\tilde{\boldsymbol{\Sigma}}$ according to the \mathcal{S} , \mathcal{F} , \mathcal{B} and \mathcal{T} subscripts. Deriving the conditional distributions for Equation (11) results in a multivariate normal posterior predictive distribution for the test shape smooth operators $\mathbf{f}_T | \mathbf{y} \sim \mathcal{N}(\boldsymbol{\mu}^*, \boldsymbol{\Sigma}^*)$, where

$$\begin{aligned} \boldsymbol{\mu}^* &= \boldsymbol{\Sigma}_{TS}(\boldsymbol{\Sigma}_{SS} + \tau^2 \mathbf{I})^{-1} \mathbf{y} \\ \boldsymbol{\Sigma}^* &= \boldsymbol{\Sigma}_{TT} - \boldsymbol{\Sigma}_{TS}(\boldsymbol{\Sigma}_{SS} + \tau^2 \mathbf{I})^{-1} \boldsymbol{\Sigma}_{ST} \end{aligned} \quad (12)$$

Note that in many applications, covariance functions can be indexed by a bandwidth or length-scale parameter θ , $\sigma_\theta(\mathbf{u}, \mathbf{v})$. For example, the Gaussian kernel can be specified as $\sigma_\theta(\mathbf{u}, \mathbf{v}) = \exp\{-\|\mathbf{u} - \mathbf{v}\|^2 / 2\theta\}$.

This bandwidth parameter can be inferred; however, posterior inference over θ is slow, complicated, and often mixes poorly [39]. For simplicity, we will work with a fixed bandwidth that is chosen via 10-fold cross validation.

4 Application: Predicting Clinical Outcomes in Glioblastoma

To fully illustrate the utility of the SECT topological summary statistic, we apply the GP regression model to a glioblastoma multiforme (GBM) radiomic study with two measured clinical outcomes: disease free survival (DFS) and overall survival (OS). One of the main aims in radiomics is determine the relationship between clinical imaging and phenotypic/clinical variation. The aggressive nature of GBM, coupled with the necessity for invasive surgical procedures, makes it difficult to obtain molecular data on the disease. Imaging technologies provide a useful alternative data source, and can help with both the earlier detection and monitoring of tumors.

Some recent work in radiomics have confirmed the utility of imaging data in GBM research. These efforts suggest that the inclusion of shape information improves both the prediction of patient survival outcomes, as well as the classification of tumor subtypes [40–43]. It is important to distinguish, however, that most of these previous studies were limited to gross spatial features of cancer images (e.g. the presence of multifocal tumors, the location of recurrent lesions, or crude volumetric calculations). The SECT offers a novel contribution to radiomic research as a topological representation of imaging data. In this section, we will specifically assess whether topological features are better predictors of DFS and OS prognoses than three other tumor characteristics: (i) gene expression, (ii) tumor morphometry, and (iii) tumor geometry.

4.1 Genomic and Radiomic Data

Magnetic resonance images (MRIs) of primary GBM tumors were collected from $n = 48$ patients archived by The Cancer Imaging Archive (TCIA) [1, 2], which is a publicly accessible data repository containing medical images of cancer patients with matched genomic and clinical data collected by The Cancer Genome Atlas (TCGA) [3]. These patients were selected based on two sets of criteria, namely: (i) individuals had post-contrast T1 axial (transverse) MRIs taken at the time of their diagnosis, and (ii) these patients have matching (mRNA) gene expression data and clinical correlates (e.g. recorded DFS and OS) that are publicly available [44, 45]. There are two key factors that influenced our decision to use this particular subset of samples. First, the T1-weighted MRI with gadolinium contrast is one of the most commonly-used imaging modalities often implemented to assay lesions with vascular activity [46]. Furthermore, axial (transverse) were considered as this was the most common representation in TCIA database and resulted in the dataset with the most observations. Second, exclusively using MRIs taken at the time of diagnosis allows us to avoid any potential confounding factors related to treatment effects that may manifest on postoperative imaging [43]. Note that considering patients that have undergone different treatment regimens could introduce false positives into the model, particularly when analyzing their gene expression levels.

Each collection of patient MRIs consisted of approximately 23-25 segmented slices of two-dimensional greyscale images (with the exact numbers varying between patients). We segment these images with a computer-assisted program to extract tumor lesions from the surrounding brain tissue [47]. Briefly, this algorithm first converts MRI images to a grayscale, and then thresholds to generate binary images. Morphological segmentation is then applied to delineate connected components. This is done by selecting contours corresponding to enhanced tumor lesions, which are lighter than healthy brain tissue. For instance, necrosis (or H_1 or H_2 homology as described above in Section 2.2) presents as dark regions nested within the indicated lesion. An example of the raw image obtained from TCIA is given in Figure 3(a), while the final segmented result is given in Figure 3(b).

From these segmented images we collect three types of tumor shape information: morphometric features, geometric measurements, and topological summary statistics. Here, we use the same morphometric features outlined in previous imaging studies [48, 49] (see listed references for specific details on extraction and computation). The final data set consisted of these 212 morphometric predictors corresponding to shape and texture, including cellularity skewness, cytoplasm intensity, nucleus texture, nucleus curvature, and median edge length. We also consider 5 tumor geometric measures. The first is the enhancing volume for each MRI slice, which is summed over lesions in the multifocal case. The other geometric measurements are the core volume of the enhancing and necrotic regions, the longest lesion diameter, and the shape factor of the tumor. For the purposes of this study, we define the shape factor to be the longest lesion diameter divided by the diameter of a sphere with the same volume. Lastly, when computing the topological summary statistics, we use 100 sublevel sets per slice and compute a different EC curve for 72 directions evenly sampled over the interval $[0, 2\pi]$. After concatenation, this results in 7200-dimensional vectors for each patient. Averaging over these curves for each direction gives the proposed smooth EC statistics. It is well known that reconstructing 3D brain tissue (and corresponding tumors) from 2D slices is a nontrivial task [50–52]. Moreover, in the context of our case study, it is not even guaranteed that the space in-between individual slices will be the same for each patient. Therefore, we aggregate topological summaries across slices for each direction as a proxy for rotating (accurate) 3D representations of each tumor.

Lastly, we use matched mRNA gene expression levels of the preselected TCGA samples as a baseline data source. Following specific preprocessing steps from other genomic studies [53], we use the robust multiarray average (RMA) normalization procedure to correct for potential lab-based batch effects and other potential confounders [54]. This resulted in a final data set consisting of 8725 genes, which also passed a pre-specified hybridization accuracy threshold and showed reasonably varying expression across the assay.

4.2 Prediction Results

We now compare the each data types ability to predict two clinical outcomes: disease free survival (DFS) and overall survival (OS). Briefly, DFS is the period after a successful treatment during which there are no signs or symptoms of the cancer; while, OS is tabulated as the entire period after the initial treatment where the patient is still alive. It is important to note that DFS is more commonly used over OS in adjuvant cancer clinical trials, because it offers earlier presentation of data [55]. This stems from the idea that events due to disease recurrence occur earlier than death from disease, thus resulting in a cleaner signal [56].

Each tumor feature type is modeled with the GP regression model detailed in Section 3. In the context of this application, every patient in the data has an official death time. Hence, there is no need for a right-censored analysis or Cox-based method [57–59]. We use two types of metrics to assess prediction accuracy: (i) the squared correlation coefficient (R^2), and (ii) the frequency for which a given data type exhibits the lowest RMSEP, which we denote as Optimal%. When analyzing each outcome, we randomly split the data 1000 different times into 80% training and 20% out-of-sample test sets. In each case, the survival times are centered and scaled to have mean 0 and variance 1 to facilitate the interpretation of results. In order to illustrate the robustness of the SECT, we apply the GP regression framework while using three different covariance functions. The goal is to show that the power of the SECT summary statistic is robust to this choice. Here, suppose that \mathbf{u} and \mathbf{v} are two different covariate vectors. We consider the linear (gram) kernel $\sigma(\mathbf{u}, \mathbf{v}) = \mathbf{u}^T \mathbf{v} / p$ where p is the length of the feature vector for a given data type, the Gaussian kernel $\sigma_\theta(\mathbf{u}, \mathbf{v}) = \exp\{-\|\mathbf{u} - \mathbf{v}\|^2 / 2\theta\}$, and the Cauchy kernel $\sigma_\theta(\mathbf{u}, \mathbf{v}) = (1 + \theta\|\mathbf{u} - \mathbf{v}\|^2)^{-1}$. Once again notice that the last two functions are indexed by a bandwidth or length-scale parameter θ , which we select via 10-fold cross-validation over the grid $[0.1, 10]$ with step sizes equal to 0.1. Briefly, a value of 0 denotes a rigid function, while 10 represents a smoothed estimator. Prediction results for all kernels are depicted in Figure 4. In Table 1, we present the mean R^2 and corresponding standard errors

across testing splits to show how each tumor characteristic performs while taking into account variability. This table also lists the estimated bandwidths that generated these results.

Overall, our study shows that the SECT topological summaries result in the most accurate predictions for survival — particularly DFS. For example, using the Cauchy kernel function with SECT features resulted in the greatest R^2 for both DFS and OS at 0.212 and 0.113, respectively. This led to the SECT being the optimal tumor characteristic 52.7% of the time for DFS and 41.7% of the time for OS. There are a few possible explanations for these results. Gene expression is known to be highly variable, particularly in GBM [60], while physical and shape traits of tumors are comparatively more stable. Thus, volumetric, morphometric, and topological features have a natural advantage. In our application, the robustness of the SECT to choice of metric is particularly relevant because the geometric structure of the brain is known to be fibrous — meaning that the brain is made up of, and connected by, cerebral fiber pathways [61]. This brings into question the validity of assuming the usual Euclidean metric when quantifying shape. Both volumetric and morphometric analyses require the specification of a metric and, in the case where the usual assumption of a Euclidean measure does not apply, an appropriate one must be constructed — which is not always a straightforward task. Moreover, in fibrous settings, there is also the possibility for the further requirement of defining a geodesic. Examining topological properties, as opposed to metric-based properties, bypasses these technical difficulties. Altogether, incorporating a topological measure that is not based on a metric results in the flexibility to compare tumors of different sizes more seamlessly. Subsequently, this also implicitly allows for comparisons between different stages of the disease without needing to account for time of progression. We hypothesize that these flexible characteristics favor the SECT as a better predictor of prognosis and survival.

These predictive results may also be due to the nature of the clinical outcomes that we chose to model. As previously mentioned, DFS is a prognostic measure of cancer recurrence and corresponds to the reappearance of the disease after initial treatment. This correlate can often be better defined than OS, where the cause of a patient’s death may not necessarily be due to cancer-based complications. Indeed, each of the tumor characteristics that we consider generally perform better when predicting DFS versus OS (again see Figure 4 and Table 1). Nonetheless, measurements that detail information on the aggressiveness of the disease (e.g. volumetric and morphometric quantities) are not as relevant as those that distinguish between the sheer existence of malignancies. Thus, topological features are effective predictors as they detail the presence of tumors.

4.3 More Biological Implications

One key implication from our results in DFS is that there possibly exist correlations between the topology of tumors and the molecular heterogeneity arising from the activation of different recurrence mechanisms. An example of this relationship occurs in (multifocal) tumors where lesions on opposite hemispheres of the brain originate from the same oncogenic effects, but events like therapeutic resistance or cancer recurrence happen in only one hemisphere. This variation can be clinically relevant. It was recently proposed that these type of topologically-based traits are linked to the mutation status of certain oncogenic relapse drivers [62]. Hence, there is growing evidence that potential pathways of progression in GBM should go beyond the simple consideration of physical proximity (i.e. closeness in a geometric sense). For instance, a particular path to recurrence in GBM may be due to ambient effects inherent to a particular hemisphere of the brain. The prediction results we present in this work suggest that the topological features extracted by the SECT may be better than simple geometric summaries at providing insight into biological phenomena at the molecular level.

5 Discussion

In the present study, we sought to quantify images of GBM tumors given by MRIs for statistical analyses. To this end, we developed a topological summary statistic transform which maps shapes into a space that admits an inner product structure that is amenable to standard functional and nonlinear regression models. We then used our summary transform to predict the survival of GBM patients using our specified functional Gaussian process regression model. In this application, we compared the predictive accuracy using both molecular biomarkers and shape covariates. The SECT was shown to explain more of the variance in DFS of patients than all other covariates in a wide variety of models defined by various kernel functions. For the Gaussian and Cauchy kernels, in particular, the SECT outperformed the other measures in accounting for the variance in both DFS and OS.

Despite these results, several interesting future directions and open questions still remain. For example, in the current study, we focus solely on measuring how well topological features predict survival. Many studies in the radiomics space use deep learning approaches for accurate classification and prediction-based tasks [63–66]. Unfortunately, in this work, we did not have access to data with large enough sample sizes for the effective training of neural networks. However, in the future, it would be useful to see how our topological summary statistics may be integrated within deep learning frameworks. To ensure power, utilizing protected data from current consortium studies with a large number of participants would be of high interest [67–69]. Moving away from prediction, it would also be useful to infer which particular spatial regions of the tumor are most relevant to clinical outcomes. Standard variable selection methods can be used to infer the directions and segments of the Euler curves that are most relevant. An important open problem is to recover, or partially reconstruct, a shape from the SECT summary statistics. Similarly, the distance measure for the SECT stated in Equation (8) provides a framework for comparing the shapes of tumors, and correlating geometric properties with molecular and clinical features. Understanding the relationship between therapeutic strategies, signaling pathway dependence, and tumor shapes would provide useful information about different forms of GBM and their etiologies. We conjecture that greater general knowledge about tumor shape may help in distinguishing true progression from pseudoprogression. Progression here meaning the growth of the tumor itself, while in pseudoprogression the tumor is infiltrated by immune cells and other factors.

Data Availability

The results shown here are in whole or part based upon data generated by the TCGA Research Network (<http://cancergenome.nih.gov/>). DICOM formatted MRI scans and patient clinical information were taken directly from the TCIA web portal (<https://wiki.cancerimagingarchive.net/display/Public/TCGA-GBM>). Matched molecular data were downloaded directly from the Genomic Data Commons (GDC) by selecting the RNA-Seq tab option (<https://portal.gdc.cancer.gov/projects/TCGA-GBM>). Shape-based summary statistics necessary for replicating this study (i.e. the segmented tumor images, the volumetric measurements, morphometric data, and topological summary statistics) are also publicly available on the Rabadán Lab GitHub repository.

Software Availability

Software to compute the SECT from images is publicly available in both R code and located on the repository <https://github.com/RabadanLab/SECT>. The MRI images were segmented using the Medical Imaging Interaction Toolkit with augmented tools for segmentation (MITKats), which was written C++ and is also located at <https://github.com/RabadanLab/MITKats> [47]. The Gaussian process regression model was fit using utilities from the Bayesian approximate kernel regression (BAKR) software package located at <https://github.com/lorinanthony/BAKR> [70].

Acknowledgements

LC would like to acknowledge the support of start up funds from Brown University. LC, AM, and RR are supported by the National Cancer Institute Physical Sciences–Oncology Network (NCI PS–ON) under Grant No. 5U54CA193313-02; AM is the PI on Pilot Grant Subaward No. G11124 for research on radiomics and radiogenomics. LC would like to acknowledge the support of start up funds from Brown University. AXC is supported by the Columbia University Medical Scientist Training Program (MSTP). SM would like to acknowledge the support of grants NSF IIS-1546331, NSF DMS-1418261, NSF IIS-1320357, NSF DMS-1045153, and NSF DMS-1613261. This work used a high-performance computing facility partially supported by grant 2016-IDG-1013 (“HARDAC+: Reproducible HPC for Next-generation Genomics”) from the North Carolina Biotechnology Center. The authors wish to thank Mao Li (Donald Danforth Plant Science Center) and Christoph Hellmayr (Duke University) for help with the formulation of code, as well as Francesco Abate (McKinsey & Co.), Katharine Turner (Swiss Federal Institute of Technology), and Jiguang Wang (Hong Kong University of Science and Technology) for helpful conversations and input on a previous version of the manuscript. The authors would also like to acknowledge The Cancer Imaging Archive (TCIA) and The Cancer Genome Atlas (TCGA) initiatives for making the imaging and the clinical data used in this study publicly available. Any opinions, findings, and conclusions or recommendations expressed in this material are those of the author(s) and do not necessarily reflect the views of any of the funders.

Author Contributions Statement

LC, AM, SM, and RR conceived the study. LC and AM developed the methods. LC, AM, and AXC developed the algorithms. LC implemented the software and performed the analyses. All authors wrote and revised the manuscript.

Competing Financial Interests

The authors have declared that no competing interests exist.

Appendix

In this section, we provide more formal details on the mathematics underlying the concepts of persistent homology and topological data analysis (TDA) for shapes and images introduced in the main text. For a complete discussion on the underlying theory in TDA and applied topology, the interested reader may refer to a detailed literature [71–73].

Homology, Simplicial Complexes, and Persistence

Homology groups provide an algebraic structure for studying holes in a topological space. These holes are captured indirectly by collecting information on what surrounds them (i.e. homology is concerned with studying the boundaries of holes). The fundamental property underlying homology is that the boundary of a boundary is necessarily zero. The term algebraicity refers to group operations and maps that relate topologically-meaningful subsets of a space with one another. In discretizing a general topological space and studying its simplicial homology, the underlying object of study is a simplicial complex. This is the context from which we work in this paper, and what will be described in detail in this section.

A k -simplex is the convex hull of $k + 1$ affine independent points v_0, v_1, \dots, v_k , and is denoted by $\sigma = [v_0, v_1, \dots, v_k]$. Examples of k -simplices are points, lines, and triangles. The 0-simplex $[v_0]$ is the vertex v_0 , the 1-simplex $[v_0, v_1]$ is the edge between the vertices v_0 and v_1 , and the 2-simplex $[v_0, v_1, v_2]$ is the triangle bordered by the edges $[v_0, v_1]$, $[v_1, v_2]$ and $[v_0, v_2]$.

Definition A1. A geometric simplicial complex K is a countable set of simplices such that:

1. Every face of a simplex in K is also in K ;
2. If two k -simplices σ_1, σ_2 are in K , then their intersection is either empty or a face of both σ_1 and σ_2 .

Fix a dimension k and a field \mathbb{F} . Given a shape M with a finite simplicial complex representation (mesh) K , a *simplicial k -chain* is a linear combination of k -simplices $\sum_k c_k \sigma_k$, where $c_k \in \mathbb{F}$ and $\sigma_k \in K$. Here, the sum is taken over all possible k -simplices. Denote the set of all such k -chains by $C_k(K)$. These k -chains may be added together (given $c = \sum_k c_k \sigma_k$ and $d = \sum_k d_k \sigma_k$, define $c + d := \sum_k (c_k + d_k) \sigma_k$) and multiplied by scalars. Thus, $C_k(K)$ is a vector space over \mathbb{F} of k -chains in K — the set of k -simplices forms a canonical basis for $C_k(K)$.

The theory and results developed in this paper rely on the simplifying assumption that \mathbb{F} is the binary field $\mathbb{Z}_2 = \mathbb{Z}/2\mathbb{Z}$. In this case, a k -chain is a collection of k -simplices, and the *boundary* of a k -simplex is the sum of its $(k - 1)$ -dimensional faces. Let $\sigma = [v_0, v_1, \dots, v_k]$ denote the simplex spanned by the specified vertices. The *boundary map* $\partial_k : C_k(K) \rightarrow C_{k-1}(K)$ maps a k -chain to a $(k - 1)$ -chain, and is given by

$$\partial_k([v_0, v_1, \dots, v_k]) = \sum_{j=0}^k [v_0, \dots, v_{-j}, \dots, v_k]$$

with linear extension, where v_{-j} denotes the dropped element j . Elements of $B_k(K) := \text{im } \partial_{k+1}$ are called *boundaries*, and elements of $Z_k(K) := \text{ker } \partial_k$ are called *cycles*.

Definition A2. The k^{th} homology group of M is defined by the quotient group

$$H_k(K) := Z_k(K) / B_k(K).$$

The intuition behind a homology group is that it contains information about the structure of K . The zeroth homology group $H_0(X)$ is generated by elements that represent connected components of X . For example, if X has three connected components, then $H_0(X) \cong \mathbb{Z}_2 \oplus \mathbb{Z}_2 \oplus \mathbb{Z}_2$, where \cong denotes

group isomorphism. For $k \geq 1$, the k^{th} homology group $H_k(X)$ is generated by elements representing k -dimensional “holes” or “loops” in X . A k -dimensional hole can be thought of as the result of taking the boundary of a $(k+1)$ -dimensional body. The ranks of the homology groups (i.e. the number of generators) are called the *Betti numbers*, and are denoted by $\beta_k(X) := \text{rank}(H_k(X))$. The notation $H_*(X)$ refers to all the homology groups simultaneously. In Figure A4, we display the homology of a torus constructed from a simplicial complex.

Persistent Homology

A *filtration* of simplicial complexes \mathcal{K} is an indexed, nested family of spaces $\mathcal{K} = \{K_t\}_{t=a}^b$ such that $K_{t_1} \subseteq K_{t_2}$ if $t_1 \leq t_2$. As the parameter t increases, the homology of the spaces K_t may change (e.g. components are added and merged, cycles are formed and filled up). The *persistent homology* of \mathcal{K} is denoted by $\text{PH}_*(\mathcal{K})$ and keeps track of the progression of homology groups generated by the filtration. More specifically, the persistent homology contains the information about the homology of the individual spaces $\{K_t\}$, as well as the mappings between the homology of K_{t_1} and K_{t_2} for every $t_1 \leq t_2$. Note that persistent homology is also equivalently referred to as *persistence*.

Definition A3. Let K be a filtered simplicial complex with $K_1 \subset K_2 \subset \dots \subset K_T = K$. The k^{th} persistence module derived in homology, or k^{th} persistent homology, of K is

$$\text{PH}_k(K) := \{H_k(K_t)\}_{1 \leq t \leq T} \text{ with } \{\varphi_{s,t}\}_{1 \leq s \leq t \leq T},$$

where each linear map $\varphi_{s,t} : H_k(K_s) \rightarrow H_k(K_t)$ is induced by the inclusion $K_s \hookrightarrow K_t$ for all $s \in \{1, 2, \dots, T\}$ where $s \leq t$.

Intuitively, the main idea behind persistent homology is to study homology across multiple scales. Rather than restricting ourselves to only one instance of a space, in persistent homology, we study the evolution of the topological structure over a filtration of the entire space. This amounts to beginning with a rigid proximity rule connecting observed data points, and then continuously relaxing this rule — all while studying the corresponding topological progression.

Barcodes and Persistence Diagrams

The persistence of the data is encoded in parameterizations of homology groups known as *barcodes*: collections of intervals which correspond to the lifetimes of topological features. The left endpoint of a bar is the *birth time* of an element in $\text{PH}_*(\mathcal{K})$ and can be thought of as the value of t where this element appears for the first time. Conversely, the right endpoint of a bar is the *death time* and represents the value of t where an element vanishes, or merges with another existing element.

Figure A5 illustrates the idea behind persistent homology and provides an example of a barcode [71]. In this example, ϵ corresponds to the filtration parameter value. The filtration is illustrated in the upper panels in the evolution of the simplicial complex in terms of vertices, edges, and faces that are formed with the progression of ϵ . Here, the H_0 homology captures connected components; H_1 captures cycles whose boundaries are formed by edges between vertices; and H_2 captures cycles with boundaries formed by faces. The dashed lines extending from the panels capture instances of the filtration link to the bars representing the topological features at particular values of ϵ . As ϵ progresses, we see connected components merge, cycles that form, and then fill up. The barcode summarizes the lifetimes of all topological features, classified by their homology groups, in this process. Two notable characteristics are the single connected component that persists, represented by the long H_0 bar, and the single H_2 bar representing the cycle bounded by faces. This suggests that the simplicial complex is a discretization of a torus.

Barcodes can thus be considered as summary statistics of the data generating process, as they sufficiently allow for a reduction in dimension of the ambient space. This information can alternatively be represented by a *persistence diagram*, which takes the birth and death times of each bar in a barcode as an ordered pair (\mathbf{y}) and produces a scatterplot. This then provides a multi-scale topological summary of the shape or surface. In a persistence diagram, the points lie in \mathbb{R}^2 and all the points on the diagonal $x = y$ have infinite multiplicity. The diagonal is included to allow for a well-defined metric on the space of diagrams or barcodes.

Since summary statistics are direct parallels to the invariants of a topological space, considering such topological approaches in data analytics is a way of reducing dimensionality in high-dimensional statistical problems (i.e. where the number of predictors is far greater than the number of observations).

Figures and Tables

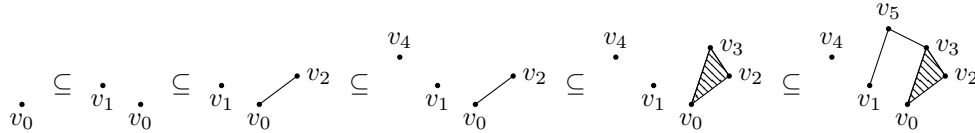


Figure 1. Demonstrating filtration of a simplicial complex K by height in direction ν . The inclusions indicate the evolution of K with the filtration, where each element (i.e. vertex, edge, and face) is included at its maximal height. For example, in the leftmost inclusion, the vertex v_0 is added and it is present in each subsequent inclusion, while the vertex v_1 emerges during the second inclusion. Similarly, the edge v_0v_2 connecting vertices v_0 and v_2 appears at the third inclusion, and the face $\langle v_0v_2v_3 \rangle$ forms at the fourth. Altogether, according to these inclusions, the collection of vertices in K are shown to evolve as follows: (i) $\langle v_0 \rangle$; (ii) $\langle v_0, v_1 \rangle$; (iii) $\langle v_0, v_1, v_2 \rangle$; (iv) $\langle v_0, v_1, v_2, v_4 \rangle$; (v) $\langle v_0, v_1, v_2, v_3, v_4 \rangle$; and at the final inclusion, (vi) $\langle v_0, v_1, v_2, v_3, v_4, v_5 \rangle$. Similarly, the collection of edges in K is said to evolve as follows: $\langle v_0v_2 \rangle$ appears at the third, $\langle v_0v_2, v_0v_3, v_2v_3 \rangle$ emerges at the fifth; and $\langle v_0v_2, v_0v_3, v_2v_3, v_1v_5, v_3v_5 \rangle$ forms at the final inclusion. This evolution of vertices, edges, and faces forms (persistence) vector spaces of i -chains, and may be written as such for concise notation (see the Appendix for further details). This figure has been previously published [12].

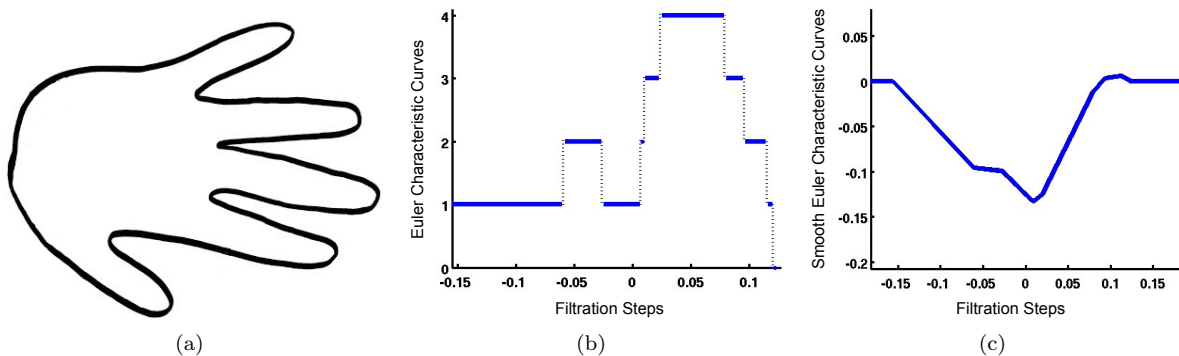


Figure 2. Example illustrating the evolutionary tracking of topological features for a given shape. Figure (a) displays a 2D contour of a hand, for which the Euler characteristic (EC) is calculated and tracked with respect to a horizontal filtration. Figure (b) then shows the Euler characteristic curve of the 2D contour. Notice that at the leftmost filtration level on the x -axis, the EC value is equal to 1 on the y -axis. This indicates one connected component corresponding to the thumb in the hand. Just before level -0.05, the index finger appears, which increases the value of the EC to 2. Figure (c) illustrates the corresponding smooth Euler characteristic (SEC) curve. This found by taking the mean value of the EC curve in (b) and subtracting it from every point along the x -axis.

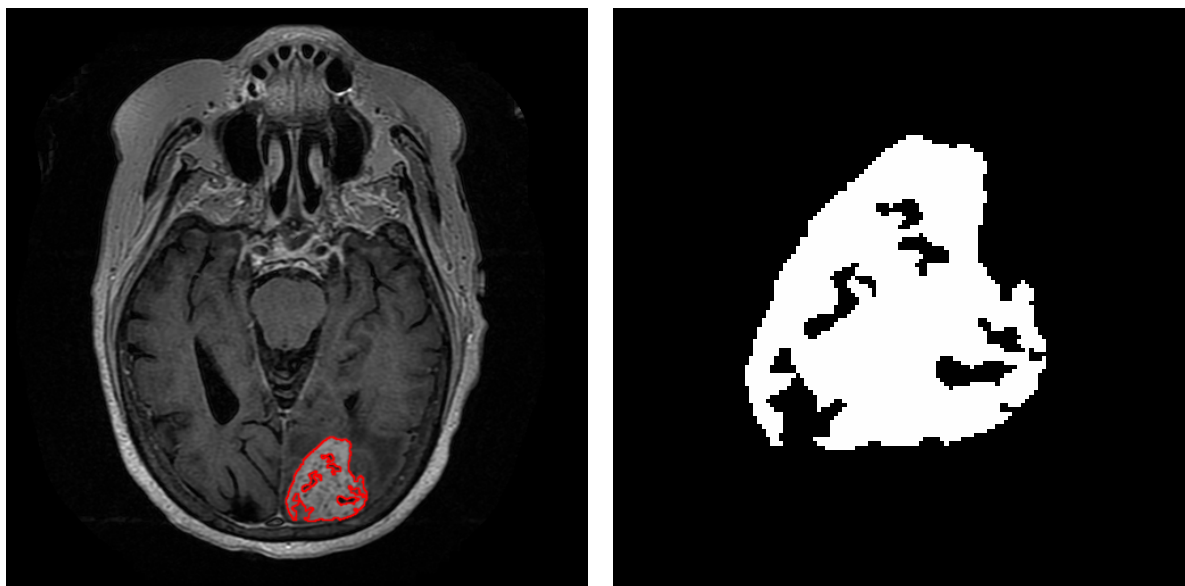


Figure 3. Example image data used in radiomic analysis. An original MRI from the TCIA and TCGA is displayed in Figure (a), while the final segmented image via the MITKats algorithm is given in Figure (b).

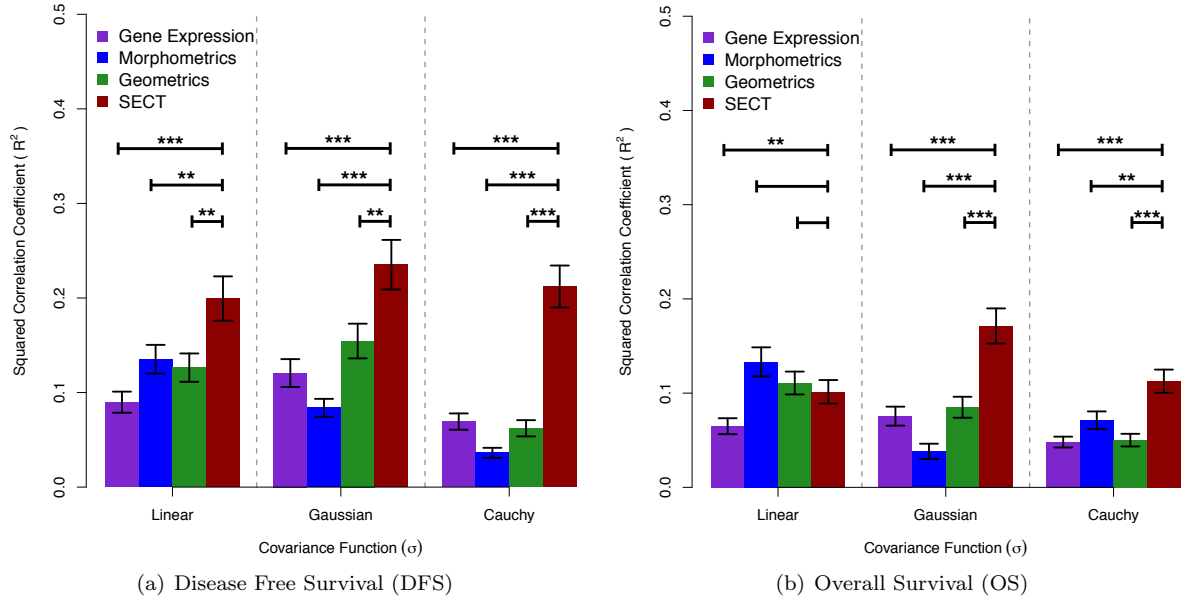


Figure 4. Results for predicting disease free survival, and overall survival using Gaussian process regression models defined by the linear, Gaussian, and Cauchy covariance functions, respectively. For each model fit, we consider the predictive utility of four different genomic data types: gene expression, tumor morphometry, tumor geometry, and the proposed smooth Euler characteristic transform (SECT). Assessment is carried out by using the predictive squared correlation coefficient R^2 , where larger numbers indicate better performance. These values are based on 1000 random 80-20 splits for each clinical outcome. Standard errors for each model are also illustrated via the vertical bars. Asterisks denote the level of significance between results via a one-sided t -test. Here the significance levels (*), (**), (***) are used for p -values satisfying $R < 1 \times 10^{-10}$, $R < 1 \times 10^{-20}$, $R < 1 \times 10^{-30}$, respectively.

Table 1. Detailed results for predicting disease free survival (DFS) and overall survival (OS) using Gaussian process regression models defined by the linear, Gaussian, and Cauchy covariance functions, respectively. For each model fit, we consider the predictive utility of four different genomic data types: gene expression, tumor morphometry, tumor geometry, and the proposed smooth Euler characteristic transform (SECT). Assessment is carried out by using the predictive squared correlation coefficient (R^2), where larger numbers indicate better performance. We also use Optimal% to denote the percentage of the time that a model exhibits the greatest R^2 . All values in bold represent the best method in these two assessment categories. These values are based on 1000 random 80-20 splits for each clinical outcome. Standard errors for each model are given the parentheses. Lastly, we also give estimates for the bandwidth or length-scale parameter $\hat{\theta}$ used to compute each kernel function. Note that $\hat{\theta}$ was found by using 10-fold cross-validation over the grid $[0.1, 10]$ with step sizes equal to 0.1.

Covariance Function(s)	Data Type	Disease Free Survival (DFS)			Overall Survival (OS)		
		R^2	Optimal%	$\hat{\theta}$	R^2	Optimal%	$\hat{\theta}$
Linear Kernel	Gene Expression	0.090 (0.010)	16.2%	—	0.065 (0.03)	13.5%	—
	Morphometrics	0.135 (0.010)	26.7%	—	0.133 (0.05)	34.5%	—
	Geometrics	0.126 (0.01)	20.9%	—	0.111 (0.04)	28.3%	—
	SECT	0.199 (0.01)	36.2%	—	0.101 (0.04)	23.7%	—
Gaussian Kernel	Gene Expression	0.121 (0.05)	22.2%	4.3	0.076 (0.03)	21.9%	10.0
	Morphometrics	0.084 (0.03)	12.8%	0.1	0.038 (0.03)	8.0%	4.0
	Geometrics	0.154 (0.06)	25.2%	5.2	0.085 (0.04)	22.1%	5.0
	SECT	0.235 (0.08)	39.8%	0.6	0.171 (0.06)	48.0%	4.2
Cauchy Kernel	Gene Expression	0.069 (0.03)	22.7%	6.4	0.048 (0.02)	16.8%	10.0
	Morphometrics	0.036 (0.02)	10.0%	1.2	0.071 (0.03)	25.6%	4.5
	Geometrics	0.062 (0.03)	14.6%	0.2	0.050 (0.02)	15.9%	3.5
	SECT	0.212 (0.07)	52.7%	0.6	0.113 (0.04)	41.7%	5.5

Supplementary Figures

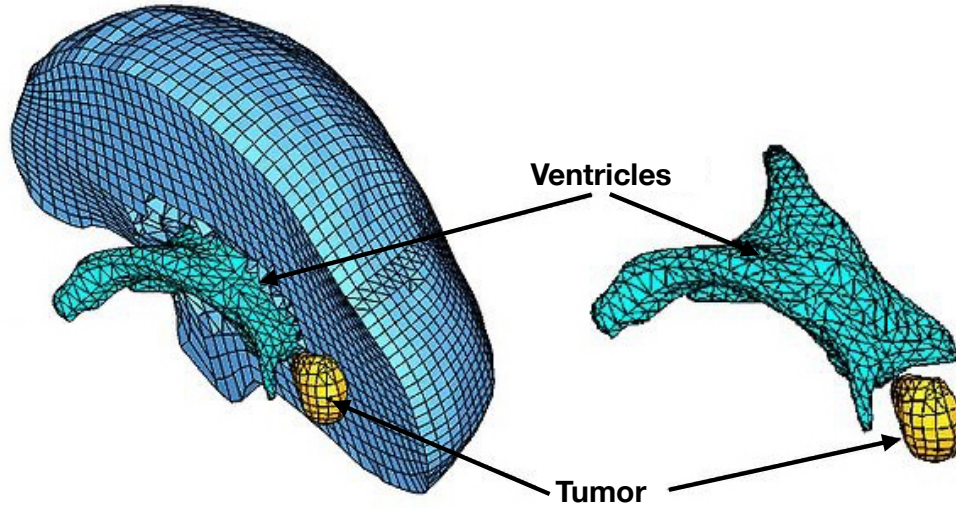


Figure A1. A mesh representation of a brain tumor and ventricles.

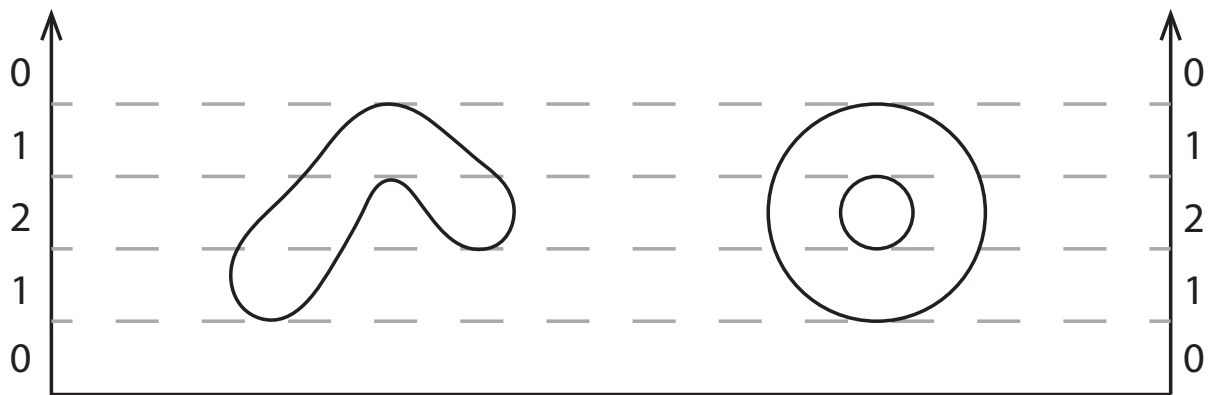


Figure A2. Counterexample for injectivity of the Euler Characteristic (EC) curve for a fixed direction. The vertical axes show the direction of the filtration for both shapes by height (i.e. the sublevel set filtration). The numbers on the axes denote the evolution of the EC for both shapes. We see that although the shapes are different, the corresponding ECs change in exactly the same manner, yielding identical ECTs for a fixed direction $\nu \in S^1$.

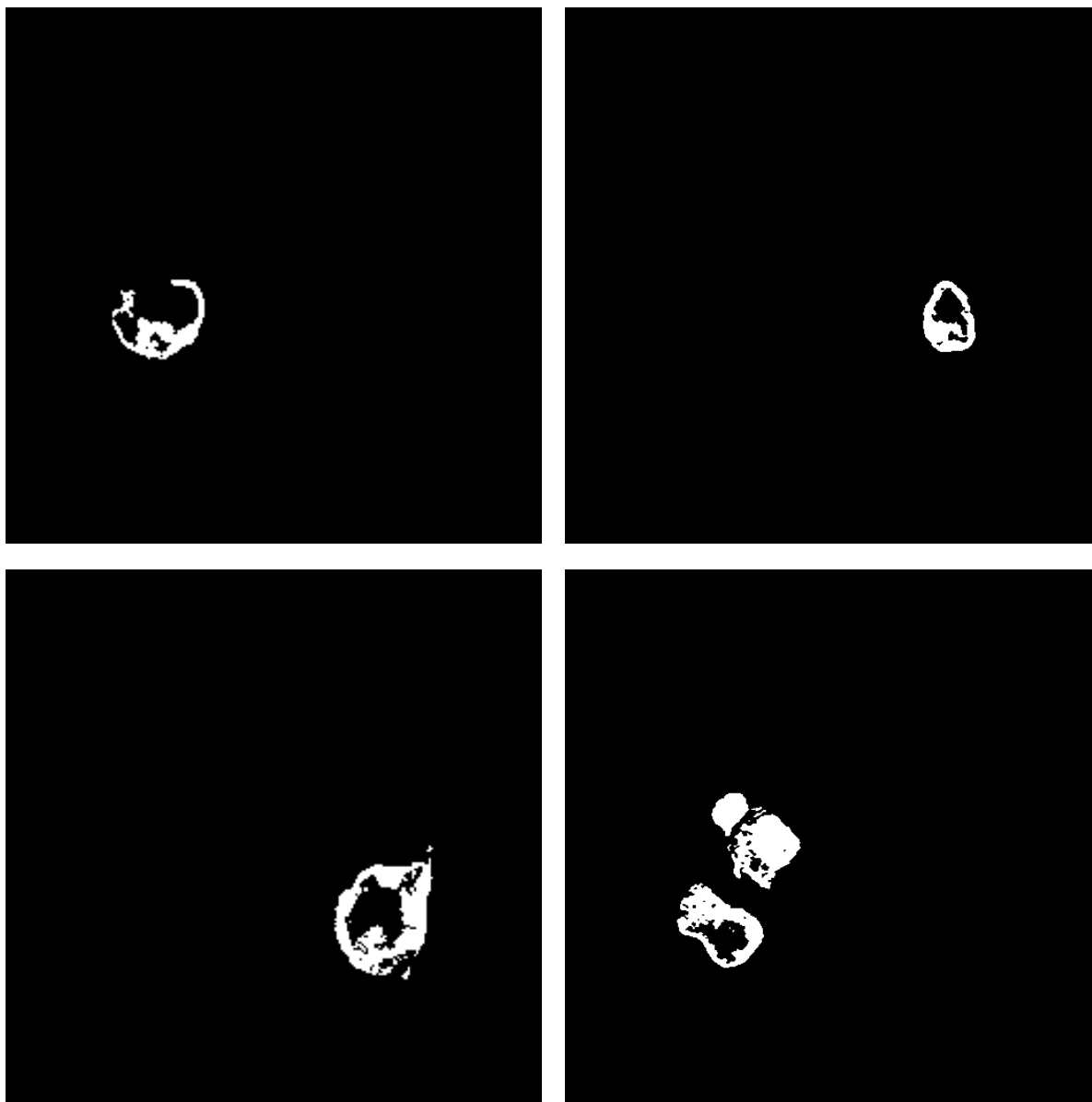


Figure A3. More examples of tumor segmentations using the MITKats algorithm. Note that all four images are taken from different patients to highlight the diversity of disease progression. These images are also examples of tumors exhibiting necrosis and multifocality.

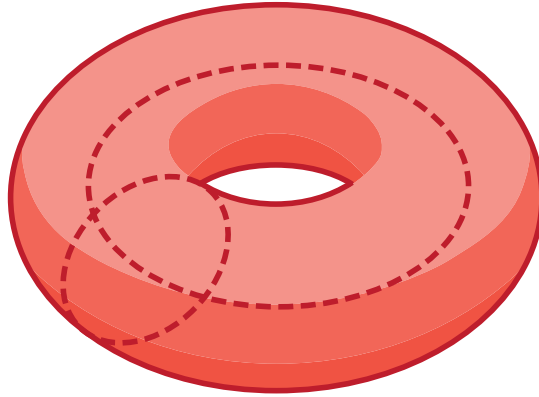


Figure A4. An illustrative example of homology using the 2-dimensional torus and its cycles. The torus has a single connected component and a single 2-cycle (the void locked inside the torus). In addition, it has two distinct 1-dimensional cycles (or closed loops) represented by the two curves in the figure. Consequently, the Betti numbers of the torus are $\beta_0 = 1, \beta_1 = 2, \beta_2 = 1$.

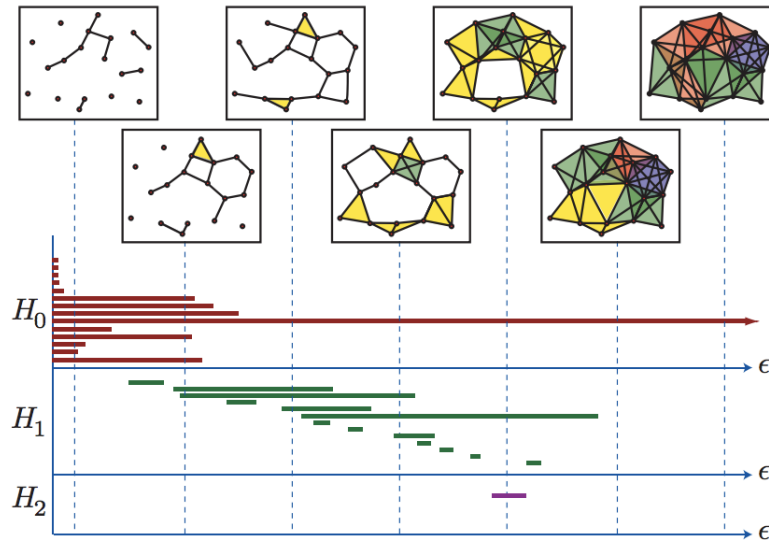


Figure A5. Illustrative example of persistent homology and the resulting barcode. In this figure, ϵ corresponds to the filtration parameter value. The filtration is illustrated in the upper panels as the evolution of a simplicial complex in terms of vertices, edges, and faces that are formed with the progression of ϵ . Here, the H_0 homology captures connected components; H_1 captures cycles whose boundaries are formed by edges between vertices; and H_2 captures cycles with boundaries formed by faces. The dashed lines extending from the panels capturing instances of the filtration link to the bars representing the topological features at particular values of ϵ . As ϵ progresses, we see connected components merge, cycles that form, and then fill up. During this process, the barcode summarizes the lifetimes of all topological features, classified by their homology groups. Two notable characteristics are (i) the single connected component that persists, represented by the long H_0 bar, and (ii) the single H_2 bar representing the cycle bounded by faces. This suggests that the simplicial complex is a discretization of a torus. This figure has been previously published [71].

References

1. Clark K, Vendt B, Smith K, Freymann J, Kirby J, Koppel P, et al. The cancer imaging archive (TCIA): maintaining and operating a public information repository. *J Digit Imaging*. 2013;26(6):1045–1057. Available from: <http://dx.doi.org/10.1007/s10278-013-9622-7>.
2. Scarpace L, Mikkelsen T, Cha S, Rao S, Tekchandani S, Gutman D, et al. Radiology data from the cancer genome atlas glioblastoma multiforme [TCGA-GBM] collection. *The Cancer Imaging Archive*. 2016;11:4.
3. The Cancer Genome Atlas Research Network. Comprehensive genomic characterization defines human glioblastoma genes and core pathways. *Nature*. 2008;455(7216):1061–1068.
4. Kendall DG. Shape manifolds, Procrustean metrics, and complex projective spaces. *B Lond Math Soc*. 1984;16(2):81–121. Available from: <http://blms.oxfordjournals.org/content/16/2/81.abstract>.
5. Bookstein FL. *Morphometric Tools for Landmark Data: Geometry and Biology*. Cambridge University Press; 1997. Available from: <https://books.google.co.in/books?id=amwT1ddIDwAC>.
6. Dryden I, Mardia K. *Statistical shape analysis*. Wiley Series in Probability and Statistics. Wiley; 1998.
7. Boyer DM, Lipman Y, St Clair E, Puente J, Patel BA, Funkhouser T, et al. Algorithms to Automatically Quantify the Geometric Similarity of Anatomical Surfaces. *Proc Natl Acad Sci U S A*. 2011;108(45):18221–18226. Available from: <http://www.pnas.org/content/108/45/18221.abstract>.
8. Lipman Y, Daubechies I. Conformal Wasserstein distances: comparing surfaces in polynomial time. *Adv Math*. 2011;227(3):1047–1077. Available from: <http://www.sciencedirect.com/science/article/pii/S0001870811000351>.
9. Al-Aifari R, Daubechies I, Lipman Y. Continuous Procrustes distance between two surfaces. *Commun Pure Appl Math*. 2013;66(6):934–964. Available from: <http://dx.doi.org/10.1002/cpa.21444>.
10. Boyer DM, Puente J, Gladman JT, Glynn C, Mukherjee S, Yapuncich GS, et al. A new fully automated approach for aligning and comparing shapes. *Anat Rec*. 2015;298(1):249–276. Available from: <http://dx.doi.org/10.1002/ar.23084>.
11. Gao T, Yapuncich GS, Daubechies I, Mukherjee S, Boyer DM. Development and assessment of fully automated and globally transitive geometric morphometric methods, with application to a biological comparative dataset with high interspecific variation. *Anat Rec*. 2018;301(4):636–658. Available from: <http://biorxiv.org/content/early/2016/11/07/086280>.
12. Turner K, Mukherjee S, Boyer DM. Persistent homology transform for modeling shapes and surfaces. *Inf inference*. 2014;3(4):310–344. Available from: <http://dx.doi.org/10.1093/imaiai/iau011>.
13. Turner K, Mileyko Y, Mukherjee S, Harer J. Fréchet means for distributions of persistence diagrams. *Discrete Comput Geom*. 2014;52(1):44–70. Available from: <http://dx.doi.org/10.1007/s00454-014-9604-7>.

14. Edelsbrunner H, Letscher D, Zomorodian A. Topological persistence and simplification. Proceedings of the 41st Annual Symposium on Foundations of Computer Science. 2000; Available from: <http://dl.acm.org/citation.cfm?id=795666.796607>.
15. Zomorodian A, Carlsson G. Computing persistent homology. *Discrete Comput Geom*. 2005;33(2):249–274. Available from: <https://doi.org/10.1007/s00454-004-1146-y>.
16. Barker FG, Davis RL, Chang SM, Prados MD. Necrosis as a prognostic factor in glioblastoma multiforme. *Cancer*. 1996;77(6):1161–1166.
17. Liu Q, Liu Y, Li W, Wang X, Sawaya R, Lang FF, et al. Genetic, epigenetic, and molecular landscapes of multifocal and multicentric glioblastoma. *Acta Neuropathol*. 2015;130(4):587–597.
18. Mileyko Y, Mukherjee S, Harer J. Probability measures on the space of persistence diagrams. *Inverse Probl*. 2011;27(12):124007. Available from: <http://stacks.iop.org/0266-5611/27/i=12/a=124007>.
19. Reininghaus J, Huber S, Bauer U, Kwitt R. A stable multi-scale kernel for topological machine learning. *Proc IEEE Comput Soc Conf Comput Vis Pattern Recognit*. 2015;p. 4741–4748.
20. Kwitt R, Huber S, Niethammer M, Lin W, Bauer U. Statistical topological data analysis - a kernel perspective. *Adv Neural Inf Process Syst*. 2015;28:3070–3078. Available from: <http://papers.nips.cc/paper/5887-statistical-topological-data-analysis-a-kernel-perspective.pdf>.
21. Kusano G, Fukumizu K, Hiraoka Y. Kernel method for persistence diagrams via kernel embedding and weight factor. *arXiv*. 2017;p. 1706.03472.
22. Edelsbrunner H, Harer J. *Computational Topology: An Introduction*. American Mathematical Soc.; 2010.
23. Müller HG, Stadtmüller U. Generalized functional linear models. *Ann Stat*. 2005;33(2):774–805. Available from: <http://projecteuclid.org/euclid.aos/1117114336>.
24. Ferraty F, Vieu P. *Nonparametric Functional Data Analysis: Theory and Practice*. Springer Science & Business Media; 2006.
25. Ramsay JO. *Functional Data Analysis*. Wiley Online Library; 2006.
26. Müller HG, Yao F. Functional additive models. *J Am Stat Assoc*. 2008;103(484):1534–1544. Available from: <http://dx.doi.org/10.1198/016214508000000751>.
27. Pomann GM, Staicu AM, Lobaton EJ, Mejia AF, Dewey BE, Reich DS, et al. A lag functional linear model for prediction of magnetization transfer ratio in multiple sclerosis lesions. *Ann Appl Stat*. 2016;10(4):2325–2348. Available from: <http://projecteuclid.org/euclid.aos/1483606862>.
28. Preda C. Regression models for functional data by reproducing kernel Hilbert spaces methods. *J Stat Plan Inference*. 2007;137(3):829–840.
29. Morris JS. Functional regression. *Annu Rev Stat Appl*. 2015;2:321–359.
30. Kadri H, Duflos E, Preux P, Canu S, Davy M. Nonlinear functional regression: a functional RKHS approach. *International Conference on Artificial Intelligence and Statistics*. 2010;p. 374–380.
31. Wang JL, Chiou JM, Müller HG. Functional data analysis. *Annu Rev Stat Appl*. 2016;3:257–295.

32. Wahba G. Support vector machines, reproducing kernel Hilbert spaces and the randomized GACV. *Adv Neural Inf Process Syst.* 1997;6:69–87.
33. Pillai NS, Wu Q, Liang F, Mukherjee S, Wolpert R. Characterizing the function space for Bayesian kernel models. *J Mach Learn Res.* 2007;8:1769–1797.
34. Yuan M, Cai TT. A reproducing kernel Hilbert space approach to functional linear regression. *Ann Stat.* 2010;38(6):3412–3444.
35. Friston K, Phillips J, Chawla D, Buchel C. Nonlinear PCA: characterizing interactions between modes of brain activity. *Philos Trans R Soc Lond B.* 2000;355(1393):135–146.
36. Mercer J. Functions of positive and negative type and their connection with the theory of integral equations. *Philos Trans R Soc Lond A.* 1909;209:415–446.
37. Rasmussen CE, Williams CKI. *Gaussian Processes for Machine Learning.* Cambridge, MA: MIT Press; 2006.
38. Kolmogorov AN, Rozanov YA. On strong mixing conditions for stationary Gaussian processes. *Theory Probab Its Appl.* 1960;5(2):204–208.
39. Liang F, Mao K, Mukherjee S, West M. Nonparametric Bayesian kernel models. Department of Statistical Science, Duke University; 2009.
40. Gutman DA, Cooper LAD, Hwang SN, Holder CA, Gao J, Aurora TD, et al. MR imaging predictors of molecular profile and survival: multi-institutional study of the TCGA glioblastoma data set. *Radiology.* 2013;267(2):560–569. Available from: <http://dx.doi.org/10.1148/radiol.13120118>.
41. Mazurowski MA, Desjardins A, Malof JM. Imaging descriptors improve the predictive power of survival models for glioblastoma patients. *Neuro-Oncology.* 2013;15(10):1389–1394. Available from: <http://neuro-oncology.oxfordjournals.org/content/early/2013/08/01/neuonc.nos335.abstract>.
42. Gevaert O, Mitchell La, Achrol AS, Xu J, Echegaray S, Steinberg GK, et al. Glioblastoma multiforme: exploratory radiogenomic analysis by using quantitative image features. *Radiology.* 2014;273(1):131731. Available from: <http://www.ncbi.nlm.nih.gov/pubmed/24827998>.
43. Macyszyn L, Akbari H, Pisapia JM, Da X, Attiah M, Pigrish V, et al. Imaging patterns predict patient survival and molecular subtype in glioblastoma via machine learning techniques. *Neuro-Oncology.* 2016;18(3):417–425. Available from: <http://neuro-oncology.oxfordjournals.org/content/18/3/417.abstract>.
44. Gao J, Aksoy BA, Dogrusoz U, Dresdner G, Gross B, Sumer SO, et al. Integrative analysis of complex cancer genomics and clinical profiles using the cBioPortal. *Sci Signal.* 2013;6(269):pl1. Available from: <http://stke.sciencemag.org/content/6/269/pl1.abstract>.
45. Grossman RL, Heath AP, Ferretti V, Varmus HE, Lowy DR, Kibbe WA, et al. Toward a shared vision for cancer genomic data. *N Engl J Med.* 2016;375(12):1109–1112. Available from: <https://doi.org/10.1056/NEJMp1607591>.
46. Adin ME, Kleinberg L, Vaidya D, Zan E, Mirbagheri S, Yousem DM. Hyperintense dentate nuclei on T1-weighted MRI: relation to repeat gadolinium administration. *Am J Neuroradiol.* 2015;36(10):1859–1865. Available from: <http://www.ajnr.org/content/36/10/1859.abstract>.

47. Chen AX, Rabadán R. A fast semi-automatic segmentation tool for processing brain tumor images. In: Holzinger A, Goebel R, Ferri M, Palade V, editors. *Towards Integrative Machine Learning and Knowledge Extraction*. Cham: Springer International Publishing; 2017. p. 170–181.
48. Han J, Chang H, Andarawewa K, Yaswen P, Barcellos-Hoff MH, Parvin B. Multidimensional profiling of cell surface proteins and nuclear markers. *IEEE/ACM Trans Comput Biol Bioinformatics*. 2010;7(1):80–90. Available from: <http://dx.doi.org/10.1109/TCBB.2008.134>.
49. Chang H, Fontenay GV, Han J, Cong G, Baehner FL, Gray JW, et al. Morphometric analysis of TCGA glioblastoma multiforme. *BMC Bioinform*. 2011;12(1):484. Available from: <http://dx.doi.org/10.1186/1471-2105-12-484>.
50. Cline HE, Dumoulin CL, Hart HRJ, Lorensen WE, Ludke S. 3D reconstruction of the brain from magnetic resonance images using a connectivity algorithm. *Magn Reson Imaging*. 1987;5(5):345–352.
51. Amruta A, Gole A, Karunakar Y. A systematic algorithm for 3-D reconstruction of MRI based brain tumors using morphological operators and bicubic interpolation. In: *2010 2nd International Conference on Computer Technology and Development*; 2010. p. 305–309.
52. Jaffar MA, Zia S, Latif G, Mirza AM, Mehmood I, Ejaz N, et al. Anisotropic diffusion based brain MRI segmentation and 3D reconstruction. *Int J Comput Int Sys*. 2012;5(3):494–504. Available from: <https://doi.org/10.1080/18756891.2012.696913>.
53. Singleton KR, Crawford L, Tsui E, Manchester HE, Maertens O, Liu X, et al. Melanoma therapeutic strategies that select against resistance by exploiting MYC-driven evolutionary convergence. *Cell Reports*. 2017;21(10):2796–2812. Available from: <https://doi.org/10.1016/j.celrep.2017.11.022>.
54. Irizarry RA, Hobbs CB, Beazer-Barclay YD, Antonellis KJ, Scherf U, Speed TP. Exploration, normalization, and summaries of high density oligonucleotide array probe level data. *Biostatistics*. 2003;2(4):249–264.
55. Sargent D, Wieand H, Haller D, Gray R, Benedetti J, Buyse M, et al. Disease-free survival versus overall survival as a primary end point for adjuvant colon cancer studies: Individual patient data from 20,898 patients on 18 randomized trials. *J Clin Oncol*. 2005;23(34):8664–8670.
56. Birgisson H, Wallin U, Holmberg L, Glimelius B. Survival endpoints in colorectal cancer and the effect of second primary other cancer on disease free survival. *BMC Cancer*. 2011;11(1):438. Available from: <http://dx.doi.org/10.1186/1471-2407-11-438>.
57. Rutledge WC, Kong J, Gao J, Gutman DA, Cooper LAD, Appin C, et al. Tumor-infiltrating lymphocytes in glioblastoma are associated with specific genomic alterations and related to transcriptional class. *Clin Cancer Res*. 2013;19(18):4951–4960.
58. Fatai AA, Gamielidien J. A 35-gene signature discriminates between rapidly- and slowly-progressing glioblastoma multiforme and predicts survival in known subtypes of the cancer. *BMC Cancer*. 2018;18:377. Available from: <http://www.ncbi.nlm.nih.gov/pmc/articles/PMC5883543/>.
59. Kundu S, Cheng Y, Shin M, Manyam G, Mallick BK, Baladandayuthapani V. Bayesian variable selection with graphical structure learning: applications in integrative genomics. *PLoS ONE*. 2018;13(7):e0195070. Available from: <https://doi.org/10.1371/journal.pone.0195070>.

60. Verhaak RGW, Hoadley KA, Purdom E, Wang V, Qi Y, Wilkerson MD, et al. Integrated genomic analysis identifies clinically relevant subtypes of glioblastoma characterized by abnormalities in PDGFRA, IDH1, EGFR, and NF1. *Cancer Cell*. 2010;17(1):98–110. Available from: <http://www.sciencedirect.com/science/article/pii/S1535610809004322>.
61. Wedeen VJ, Rosene DL, Wang R, Dai G, Mortazavi F, Hagmann P, et al. The geometric structure of the brain fiber pathways. *Science*. 2012;335(6076):1628. Available from: <http://science.sciencemag.org/content/335/6076/1628.abstract>.
62. Lee JK, Wang J, Sa JK, Ladewig E, Lee HO, Lee IH, et al. Spatiotemporal genomic architecture informs precision oncology in glioblastoma. *Nat Genet*. 2017;49(4):594–599. Available from: <http://dx.doi.org/10.1038/ng.3806>.
63. Lao J, Chen Y, Li ZC, Li Q, Zhang J, Liu J, et al. A deep learning-based radiomics model for prediction of survival in glioblastoma multiforme. *Sci Rep*. 2017;7(1):10353. Available from: <https://doi.org/10.1038/s41598-017-10649-8>.
64. Li Z, Wang Y, Yu J, Guo Y, Cao W. Deep Learning based Radiomics (DLR) and its usage in noninvasive IDH1 prediction for low grade glioma. *Sci Rep*. 2017;7:5467. Available from: <http://www.ncbi.nlm.nih.gov/pmc/articles/PMC5511238/>.
65. Bibault JE, Giraud P, Durdux C, Taieb J, Berger A, Coriat R, et al. Deep Learning and radiomics predict complete response after neo-adjuvant chemoradiation for locally advanced rectal cancer. *Sci Rep*. 2018;8(1):12611. Available from: <https://doi.org/10.1038/s41598-018-30657-6>.
66. Rathore S, Akbari H, Rozycki M, Abdullah KG, Nasrallah MP, Binder ZA, et al. Radiomic MRI signature reveals three distinct subtypes of glioblastoma with different clinical and molecular characteristics, offering prognostic value beyond IDH1. *Sci Rep*. 2018;8(1):5087. Available from: <https://doi.org/10.1038/s41598-018-22739-2>.
67. Mueller SG, Weiner MW, Thal LJ, Petersen RC, Jack C, Jagust W, et al. The Alzheimer's disease neuroimaging initiative. *Neuroimaging Clin N Am*. 2005;15(4):869–xii. Available from: <http://www.ncbi.nlm.nih.gov/pmc/articles/PMC2376747/>.
68. Gounder MM, Nayak L, Sahebjam S, Muzikansky A, Sanchez AJ, Desideri S, et al. Evaluation of the safety and benefit of phase I oncology trials for patients with primary CNS tumors. *J Clin Oncol Res*. 2015;33(28):3186–3192. Available from: <https://doi.org/10.1200/JCO.2015.61.1525>.
69. Sudlow C, Gallacher J, Allen N, Beral V, Burton P, Danesh J, et al. UK Biobank: an open access resource for identifying the causes of a wide range of complex diseases of middle and old age. *PLoS Med*. 2015;12(3):e1001779–. Available from: <https://doi.org/10.1371/journal.pmed.1001779>.
70. Crawford L, Wood KC, Zhou X, Mukherjee S. Bayesian approximate kernel regression with variable selection. *J Am Stat Assoc*. 2018; Available from: <https://doi.org/10.1080/01621459.2017.1361830>.
71. Ghrist R. Barcodes: the persistent topology of data. *Bull Amer Math Soc*. 2008;45(1):61–75. Available from: <http://dx.doi.org/10.1090/S0273-0979-07-01191-3>.
72. Carlsson G. Topology and data. *Bull Amer Math Soc*. 2009;46(2):255–308. Available from: <http://dx.doi.org/10.1090/S0273-0979-09-01249-X>.
73. Carlsson G. Topological pattern recognition for point cloud data. *Acta Numer*. 2014;23:289–368. Available from: <https://www.cambridge.org/core/article/topological-pattern-recognition-for-point-cloud-data/BB0DA0F0EBD79809C563AF80B555A23C>.